TELLUS

Dynamical structures for southwesterly airflow over southern Norway: the role of dissipation

By IDAR BARSTAD*, *Department of Geology and Geophysics, Yale University, CT, USA;*
SIGBJØRN GRØNÅS, *Geophysical Department, University of Bergen, 5007 Bergen, Norway*

ABSTRACT

Earlier studies have revealed mesoscale structures in southwesterly flows over the mountains of southern Norway (Rossby number ∼1): a left-side jet and an upstream wind minimum as signs of the influence of rotation; a downstream wind shadow connected to inertio-gravity waves; a weak jet on the right side of the wind shadow and a shallow coastal wind shadow between the left-side jet and the main wind shadow. In the present study, the dynamics of the structures have been further examined from the results of experiments performed by a mesoscale numerical model and computations using a linear model with rotation included. Ideal atmospheric conditions for a large-scale wind direction from southwest have been used to initialize the numerical model. The sensitivity of mesoscale structures was studied with respect to dissipation from wave breaking and surface friction. Nonlinearity and dissipation in breaking waves are needed to explain the location, depth and strength of the downstream wind shadow. Increased wind to the right of the shadow was found to be generated by the effect of the Coriolis force as air was pulled towards the low-pressure perturbation behind the mountains. The coastal wind shadow was found to be a direct result of differential friction between land and ocean. Nonlinear experiments and an attempt to include boundary layer effects in linear theory showed that friction is reducing the effective height of the mountain and the signal of the mesoscale structures.

1. Introduction

Prevailing southwesterly winds over southern Norway (1500 m high; 100–150 km wide) give rise to mesoscale structures formed by the mountains. In this way, the mountain flow gives large wind variations as well as variations in other meteorological quantities, e.g. orographic precipitation. In addition, mesoscale structures may trigger phenomena such as lee cyclogenesis and föhn events. In this paper, we seek improved physical understanding of the mesoscale structures. In doing so, we tie a link between theoretical work and practical weather forecasting. Accordingly, our findings will ease the interpretation of daily weather maps for flows over southern Norway and provide deeper insight in to local variations in weather and climate.

Barstad and Grønås (2005) (hereafter BG05) identified several mesoscale structures in southerly and southwesterly flows passing through southern Norway. From numerical simulations initiated with ideal flows, they found the simulated mesoscale structures to be well in accordance with wind observations along the coast and old forecasting rules. The mesoscale structures are

indicated in Fig. 1. A jet—called *the left-side jet*—was found at the left side of the mountains, and an *upstream minimum* was located at the right side of the symmetry axis (equal terrain volume on each side of the large-scale flow). These two structures highlight the asymmetric flow pattern caused by the influence of rotation on the perturbations set up by the mountains. BG05 pointed out that rotation acts to prevent upstream blocking when the flow comes from southwest. When the flow comes from southeast, however, rotation supports upstream stagnation and a tendency of blocking. Pierrehumbert and Wyman (1985) and Thorsteinsson and Sigurdsson (1996) presented congruent results.

Downstream of the highest mountain tops, two elongated wake-like phenomena were identified: a structure called *the (main) wind shadow* and a similar, shallower structure at the coast north of Stadt, called *the coastal wind shadow* (Fig. 1). The main wind shadow was found to be a result of downstream inertio-gravity waves (Trüb and Davies, 1995). The influence of dissipation (Grubišić et al., 1995; Ólafsson and Bougeault, 1997; Ólafsson, 2000) was believed to be modest. The coastal wind shadow, on the other hand, was assumed to originate from differential surface friction at the coast and upstream dissipation associated with steep mountains. An area of strong winds appeared to the right of the main wind shadow, *the right-side jet*. The signal from this structure was weak, and it was

---
*Corresponding author.
e-mail: idar@gfi.uib.no
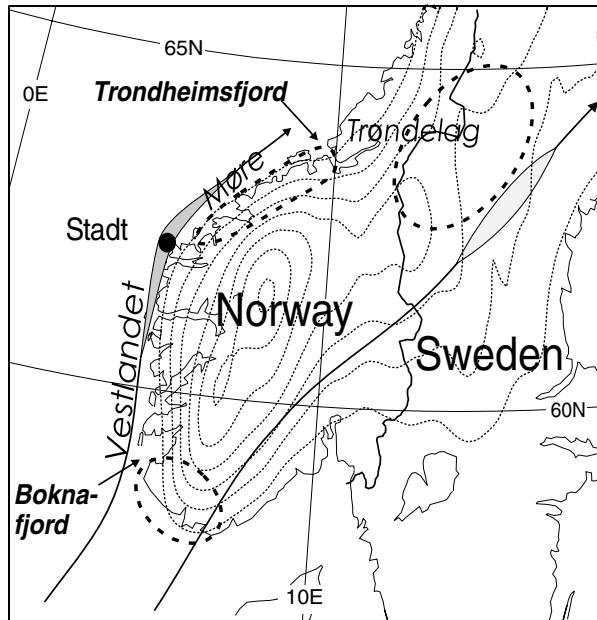Present address: Geophysical Department, University of Bergen, 5007 Bergen, Norway.

Fig 1. Inner integration area for the nonlinear model. The geographical names in the text are indicated. Typical locations of the main mesoscale features are shown. The left-side and the right-side jet are shaded, and minima (upstream minimum, downstream wind shadow and the coastal wind shadow) are indicated with broken lines. Terrain contours are indicated as thin, broken lines every 200 m, starting from 200 m above sea level.

suggested that upstream dissipation played a minor role in its formation.

In recent years, new relevant theory on flows over idealized mountains has appeared, and a review is given in Section 2. Downstream structures comparable to those found behind the mountains of southern Norway are expected to appear in areas having similar mountains, e.g. Iceland and New Zealand. Relevant studies in these areas are limited. On the other hand, several studies related to downstream structures, such as wakes and potential vorticity (PV) banners, have been carried out for higher mesoscale mountains, first of all the Alps (Schär et al., 2003, and references therein). These studies, which include mesoscale observations from designated campaigns, are found to have some relevance for the present study.

In BG05, the mentioned structures were identified and verified, sensitivity studies were limited to large-scale wind speed and direction. Although the effects of dissipation were suggested to have different influence on the structures, sensitivity studies assigned to dissipation were not carried out. In the present paper, we investigate the influence of dissipation, first of all for the downstream flow structures. This enables us to present better physical explanations for the origin of the structures.

As in BG05, the present study is based on data from experiments with the numerical mesoscale atmospheric model MM5 (Grell et al., 1994). All the present experiments have been done

for a fixed direction of the large-scale flow (southwest), a constant upstream static stability, expressed by the Brunt-Väisälä frequency, N, and without diabatic heating (dry model, no radiation, no heat fluxes from the surface). Simulations are made using the same large-scale wind speeds as in BG05 (10, 15, 22.5 ms^{-1}). For each wind speed, three experiments related to dissipation have been made: (1) a run without surface friction, where dissipation in the model is related to breaking gravity waves and nonlinear flow splitting; (2) a run with surface friction included, where surface roughness was kept constant everywhere and (3) a run with different roughness over land and sea. Signatures of dissipation were found by calculating the turbulent kinetic energy (TKE) (for theory, see Section 2). Some experiments were made with smoothed orography in order to get clearer signals of the inertio-gravity waves. In BG05, the effect of rotation was not separated from those of surface friction. In order to gain a clearer discussion, we have in this paper some experiments addressing the flow structures' sensitivity to rotation. Additionally, flow solutions using a linear Boussinesq model with rotation included eased the interpretation of the results. The linear model is described in the Appendix. The linear model was used without surface friction, but an attempt to include surface friction has been included in the discussion.

Section 3 describes the numerical model and explains the experimental setup. Section 4 presents results on effects of dissipation on the mentioned downstream mesoscale structures. Section 5 is left for discussion of the dynamics of the flow structures, followed by conclusions in Section 6.

2. Theory

BG05 found the effect of rotation to be the dominant cause of the mesoscale structures (left-side jet, upstream minimum and downstream wind shadow). The main parameter expressing the influence of rotation is $Ro = U/fL$, where U is a typical wind speed of the background flow and f the Coriolis parameter. For the typical scale, $L \sim 100$ km, of the widest mountain of southern Norway and $f = 10^{-4}$ s^{-1}, $Ro \sim 1$. In non-rotating, inviscid, hydrostatic flow, the non-dimensional height, $\hat{h} = hN/U$ is the main governing parameter for mountain flows (Smith, 1989a). Here, h is the height of the mountain. The flow setting used in BG05 gave $\hat{h} \sim 1$.

Pierrehumbert and Wyman (1985) used theory and results from a numerical model to explain the upstream influence of rotation for flows with $Ro \sim 1$ over a two-dimensional (2-D) mountain. Trüb and Davies (1995) also used flow modelling over a 2-D mountain to address the influence of rotation on the wave activity primarily behind the ridge. Thorsteinsson and Sigurdsson (1996) and Peng et al. (1995) discussed the modelled flow character for 3-D mountains. Their discussion included aspect ratios (a_x/a_y) between scales a_x and a_y perpendicular to each other forming mountains with contours shaped as ellipses.

Stably stratified flow in a non-rotating environment passing a low isolated mountain is expected to generate gravity waves. An increase in the mountain height leads to two regimes, which might co-exist (Smith, 1989a). (1) A wide—referring to aspect ratio $a_x/a_y \ll 1$, where x is along the flow direction—mountain gives exaggerated density anomalies causing steepening of waves aloft near the crest. Stagnation aloft and wave breaking result. (2) A narrow mountain leads to flow stagnation and splitting at the surface, upstream of the crest. Weaker lifting and smaller density anomalies are produced. In both regimes, dissipation is expected, and consequently PV on isentropes is not conserved.

In case of gravity wave breaking, PV dipoles result, and vortices and possibly return currents are typically found downstream in a wake area. The three-dimensionality of the problem grants flow splitting and intersection of isentropes with the lower boundary. In case there is no splitting or breaking—and no associated dissipation—PV is conserved even for highly nonlinear flows.

As dissipation takes place along a trajectory over the mountain, the Bernoulli function becomes non-conservative. Schär and Smith (1993), Schär (1993) and Schär et al. (2003) discussed the relation between the net PV flux and the gradient of the Bernoulli function, and showed that the intersection between constant Bernoulli surfaces and isentropes gave rise to PV.

Smolarkiewicz and Rotunno (1989) argued that vorticity and wake formation might take place without dissipation in the interior or diffusion inwards through the lower boundary (free-slip lower boundary condition). They argued that the vorticity is introduced through baroclinic tilting terms. Smith (1989b) disputed their view and proposed a more robust definition of wakes. According to Smith, the formation of wakes is associated with the production of PV. As a result, wake-formation cannot take place in an inviscid flow without dissipation or surface friction. As shown in Smith (2001), the baroclinic term acts like a converter from vorticity to PV when dissipative effects are present. Schneider et al. (2003) defined a generalized PV where surface PV was added to the concept of interior PV. They came to a similar conclusion: the baroclinic terms convert surface PV to internal PV in the presence of dissipation.

In case rotation becomes a significant part of the problem, it is not obvious that upstream stagnation of air will lead to a wake and a regime change. Even without stagnation, something similar to a wake, based on the definition of Smolarkiewicz and Rotunno (1989), might appear. In the results of Trüb and Davies (1995), reversed flow was found behind the ridge some distance above the surface. No accompanied upstream stagnation was found.

3. The experimental setup

We have chosen to apply two different model systems. The main system is a simplified version of the numerical model MM5 (Grell et al., 1994) used in BG05. The second system is an inviscid 3-D linear model, with rotation included.

3.1. Nonlinear model

Apart from some model simplifications, the setup of the experiments is identical to that in BG05. The model system has been run with so-called two-ways nesting with 10 and 30 km horizontal grid size in the respective model domains. The model integration has been performed on a polar stereographic mesh, and the Coriolis parameter (f) has been set constant (f plane). The chosen value is f at $60\,°N$ ($1.24 \times 10^{-4}\ s^{-1}$). The outer area had dimensions (60, 66) and the inner (100, 94) (see Figs. 1 and 7a). Vertically, the model used a relatively high resolution, 39 sigma layers with the model top at 10 hPa. Seventeen layers are found in the lower 1.2 km. Using a prognostic equation for TKE (Burk and Thompson, 1989), the model system allows turbulence to be non-local and advected. The model runs have been initiated from an ideal atmosphere where upstream wind direction has been constant from southwest (230 degrees). Static stability has been kept constant ($N = 0.012\ s^{-1}$) in the troposphere, increasing to a stronger stability in the stratosphere (above 300 hPa). The upstream wind speed has been varied.

The main simplification compared to experiments in BG05 is that the model is dry and that heat fluxes and radiation calculations have been turned off. In this way, only turbulent momentum exchange is allowed with the surface. Towards the upper boundary of the model domain, the wave activity is damped by increased viscosity using the Rayleigh-damping approach (Klemp and Lilly, 1978).

Different terrains have been used in the experiments: (1) A mountain resolved by a 10-km horizontal grid size, where wavelengths twice the grid length have been removed to avoid noise generation. The land use properties have then been the realistic ones offered by the MM5-model system. (2) A smoothed mountain prepared by transformation of the terrain into the Fourier space, filtering characteristic wave components shorter than 20 km (Gaussian smoothing). The result is shown in Fig. 1. Homogeneous surface friction has been applied (ocean type: $z_0 = 0.0001$ m). (3) Some simulations on the smoothed mountain have used differential friction between land and ocean. The intersection between ocean ($z_0 = 0.0001$ m) and land ($z_0 = 0.1$ m) has been placed at the 50-m height contour.

3.2. Linear model

The linear model includes rotation, but has no formulation of internal dissipation or any friction with the terrain. The map factor in the simulated domains has been unity; thus there is a one-to-one correspondence with regard to the two systems' underlying terrains. In the discussion, an attempt to include boundary-layer (BL) effects is described, neglecting rotation. The derivation of the linear model is found in the Appendix.

4. Results

In BG05, no upstream stagnation or flow splitting was found in southwesterly flows for upstream wind speeds down to $10 \, \mathrm{ms^{-1}}$. The result from BG05 thus implies that the influence of rotation for this direction—and possibly also surface friction—acts to hamper a regime change as the wind speed decreases towards $10 \, \mathrm{ms^{-1}}$. We start this section by adding some evidence to rotation's influence on flow regimes from a few experiments (4.1). The main item, however, is to describe the impact of internal dissipation in the flow and surface friction on the mesoscale structures, in particular on the lee side. This will be assessed by experiments with and without surface friction in flows over smoothed mountains (4.2). The importance of dissipation will be pinpointed using calculations of TKE, caused by surface friction and wave breaking. The results without surface friction (rotation included) are compared with results from a similar linear model over the smoothed terrain (4.3). Finally, results from experiments with differential friction are compared with experiments with homogeneous friction (4.4). We here concentrate on its effect on the left-side jet and the coastal wind shadow.

Table 1 defines the different experiments with respect to wind speed U, friction, rotation and topography. UXX points to the upstream wind speed, where XX is 10, 15 and $22.5 \, \mathrm{ms^{-1}}$, respectively. Some experiments have been done with smoothed topography (denoted by S) and some with full resolution (no letter); some without friction (no letter), some with homogeneous friction (f) or differential friction between sea and land (df); most experiments with rotation (no indication), a few without (nrot). Extreme wind speeds in the different experiments—defined as speed-ups U_{ex}/U, where U_{ex} is a maximum or a minimum wind speed—are shown in Table 2 for the left-side jet, the upstream minimum, the downstream wind shadow and the right-side jet.

4.1. Effect of rotation on flow regimes

In simple, non-rotating flows with no surface friction over simple mountains (e.g. a circular Gaussian mountain), a change from a flow regime characterized by mountain waves (flow-over) to a

Table 1. Definition of the different experiments with respect to rotation, terrain and friction. They all have a notation starting with UXX, where XX is one of the upstream wind speeds 10, 15 or $22.5 \, \mathrm{ms^{-1}}$

Simulation	Rotation	Real terrain	Smoothed terrain	Friction (that of the ocean)	Differential friction
UXX	x	x			
UXXnrot		x			
UXXS	x		x		
UXXfS	x		x	x	
UXXdfS	x		x		x
UXXf	x	x		x	
UXXdf	x	x			x

Table 2. Speed-up in the left-side jet, the upstream minimum, the downstream wind shadow and the right-side jet in the different experiments. Speed-up is defined as U_{ex}/U, where U_{ex} is a maximum or a minimum wind speed. The maxima are taken at the height they appear while the minima are at about 640 m above ground

Simulation	Left-side jet	Wind shadow	Right-side jet	Upstream minimum
U10	2.80	0.02	1.62	0.60
U10nrot	—	0.05	—	0.43
U10S	2.82	0.05	1.23	0.74
U10fS	2.02	0.27	1.19	0.72
U10dfS	1.95	0.25	1.21	0.70
U15	2.27	0.02	1.18	0.65
U15nrot	—	—	—	0.34
U15S	2.36	0.08	1.12	0.73
U15fS	1.73	0.36	1.12	0.70
U15dfS	1.64	0.31	1.15	0.67
U225	1.83	0.45	—	0.71
U225nrot	—	0.75	—	0.56
U225S	1.85	0.58	1.09	0.76
U225fS	1.50	0.55	1.03	0.72
U225dfS	1.44	0.43	—	0.70

regime characterized by upstream stagnation and flow splitting (flow-around) takes place when the non-dimensional mountain height is of the order of one (1.6 ± 0.2 for a Gaussian circular mountain; Smith and Grønås, 1993). In our simulations, the maximum height of the main massif is about 1500 m. When rotation is excluded and the upstream large-scale wind speed varies between 10 and $15 \, \mathrm{ms^{-1}}$ ($\hat{h} = 1.8$ and 1.2, respectively), a regime change might be expected. In order to test when such a regime transition may take place for southern Norway, we present results from four experiments without surface friction: U10nrot; U10; U15nrot and U15 (see Table 1).

Figure 2 shows the flow without rotation and friction for $U = 10 \, \mathrm{ms^{-1}}$ (U10nrot) at the surface (Fig. 2a, lowest model surface), a cross section along the flow downstream the highest mountains and a cross section across (Figs. 2b, c). A stagnation point upstream the main crest of the mountains appears as a sign of flow splitting (Figs. 2a, b). Immediately on the lee side, we find a classical wake with stagnation points (Figs. 2b, c), similar to those in experiments over idealized mountains (e.g. Smolarkiewicz and Rotunno, 1989). In agreement with theory (see Section 2), PV anomalies of different signs are found to wrap horizontally on both sides of the wake, near the lower boundary (not shown). The PV banners are associated with the production of TKE in breaking waves.

With rotation (U10), a pronounced asymmetric flow appears (Fig. 3a), with stronger winds on the left side (the left-side jet) and a wind minimum at the upstream right side of the mountains (the upstream minimum). Notably, no stagnation point is now
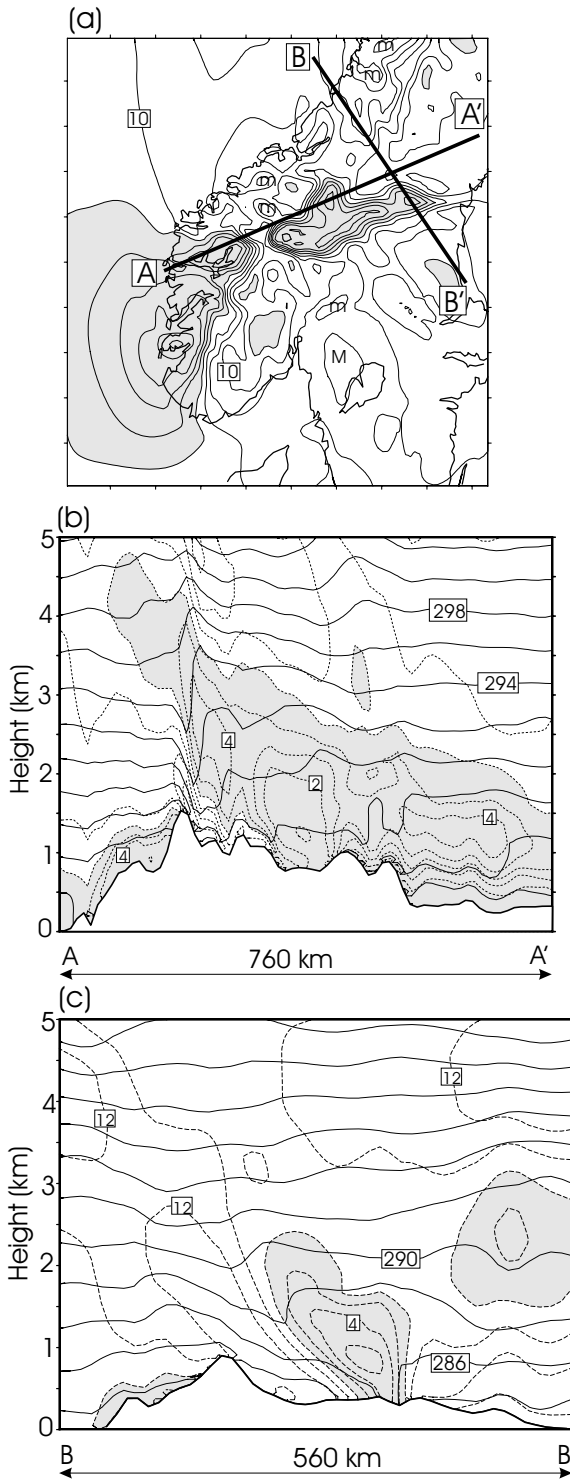
Fig 2. Wind speed (isotachs every 2 ms⁻¹) for $U = 10$ ms⁻¹ in an experiment without rotation ($f = 0$) and with realistic terrain. (a) Lowest model level. (b) Vertical cross-section along the flow (isentropes every 2 K are added) and (c) vertical cross section normal to the flow (with isentropes). Positions for the sections are given in (a). Areas with strong and weak wind speed are grey-shaded; light: below 8 ms⁻¹, and dark: above 16 ms⁻¹.
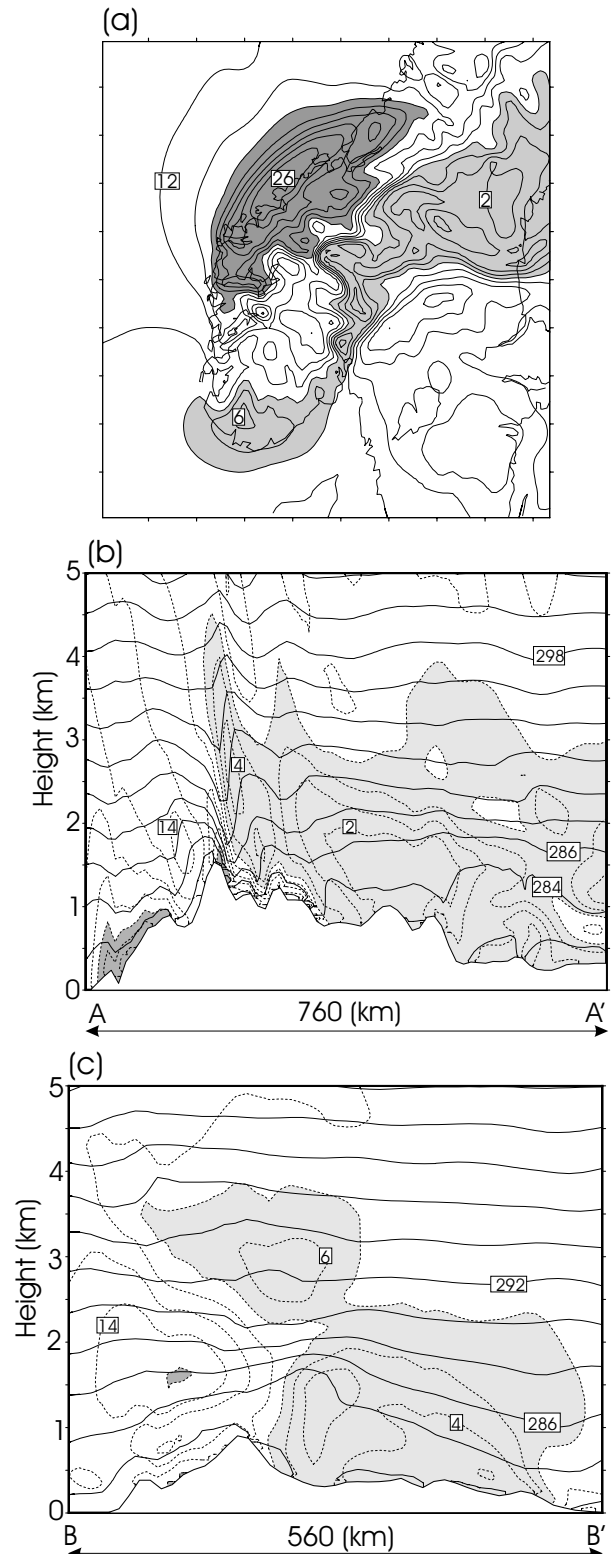

Fig 3. As Fig. 2, but for an experiment with rotation included ($f = 1.24 \cdot 10^{-4}$ s⁻¹). Positions of the cross-sections are the same as in Fig. 2.

found in this minimum (Table 2). The flow downstream of the mountains is characterized by mountain waves (inertio-gravity waves; Fig. 3b). As discussed in BG05, the waves give a wind shadow downstream the highest mountains (Figs. 3b, c). At the surface we find a band of weak winds from the upstream minimum, over eastern Norway and further northeastward towards the eastern boundary (Fig. 3a).

For stronger wind and no rotation (U15nrot), the wake disappears (not shown). However, a tendency to stagnation is still connected to the smallest resolved scale of the very highest mountains. The flow is now characterized by mountain waves only. In this way, a shift in the flow regime takes place when the wind speed is increased from 10 to 15 ms^{-1}. When rotation is included (U15), again the typical asymmetric flow response appears, much as for U10, but with smaller amplitudes (not shown, but see Table 2). No upstream stagnation is found. The band with weak winds at the surface behind the mountain is much as in U10.

With a few experiments without rotation and no surface friction, we have showed that the flow changes character from flow-around to flow-over as the background wind speed is raised from 10 to 15 ms^{-1} ($\hat{h}$ decreased from 1.8 to 1.2). The flow-around regime was first of all confirmed by a wake behind the mountain, with a character in accordance with those found by Smolarkiewicz and Rotunno (1989). This means that the regime change for the real, rather complex mountains, seems to take place at about the same non-dimensional height as for flows over simpler, idealized mountains. In this way, we have demonstrated that the non-dimensional height, computed from the highest mountain in the area, has relevance as a flow parameter in complex terrain. The results are in accordance with Ólafsson and Bougeault (1997).

When rotational effects were included, no such regime change took place. The upstream stagnation ceased to exist even for high $\hat{h}$ ($U = 10$ ms^{-1}). As explained in BG05 and in accordance with Pierrehumbert and Wyman (1985), the action of rotation helps the particles over the mountains. This means that for southwesterly flows, rotation prevents a regime change. Accordingly, all our experiments with rotation gave a regime characterized by flow over and inertio-gravity waves. As in BG05, the waves formed a rather deep area of weak winds downstream of the highest mountain; the downstream wind shadow. This means that the action of rotation produces a kind of a wake, although no flow splitting takes place. Similar results were found by Trüb and Davies (1995), Thorsteinsson and Sigurdsson (1996) for flows passing ideal mountains.

If we now consider linear flow solutions with decreasing wind speed, we may gain some insight in the increasing effect of the Coriolis force. As shown in the Appendix, the vertical wave number m is given by

$$m^2 = \frac{N^2}{(Uk)^2 - f^2}(k^2 + l^2), \tag{1}$$

where k and l are horizontal wave numbers. The vertical wave number m might be inserted in the solution for vertical displacements in Fourier space ($\hat{\eta} = \hat{h}e^{imz}$). Consider a constant wind speed U, a critical wavelength L_c exists for $Ro = 1$ ($(Uk)^2 = f^2$ in (1)). Longer waves than L_c have an evanescent, damped solution vertically. Shorter wavelengths give a wave character, i.e. a trigonometric solution of the displacements. Now, assuming a fixed typical length-scale for southern Norway of 100 km, the critical wind speed giving $Ro = 1$ is between $U = 10$ and 15 ms^{-1}. We note that this is the same range in wind speed where upstream stagnation is expected when rotation is excluded. For lower wind speeds, the effect of the Coriolis force becomes stronger and waves less frequent.

4.2. The role of surface friction

We first present two experiments with smoothed topography and rotation—U15S without surface friction and U15fS with homogeneous surface friction of the ocean. Figs. 4 and 5 present the flows in the two experiments in five similar panels a, b, c, d and e in each figure. The horizontal flow (wind vectors, wind speed) is shown at two levels (a: surface and b: upper level). The surface level is the lowest model level, and the upper level is a level approximately at the top of the BL when friction is included (layer 25, about 630 m over model terrain). Two cross sections (θ, wind speed, TKE) downstream the mountains are shown (c: along and d: across the main flow direction) for the two experiments, respectively. Positions of the cross sections are shown in Fig. 2a. The panel e shows slp and TKE at the upper level (630 m) and a level 280 m above ground.

Naturally, in both experiments the flow is characterized by a strong asymmetry (Figs. 4 and 5) due to rotation. The left-side jet has nearly the same position with maximum speeds south of Trondheimsfjord, 35.4 ms^{-1} at the surface for U15S and 26.0 ms^{-1} at the top of the BL for U15fS (see also Table 2). The upstream minimum is located on the southwestern coast (12.8 and 11.8 ms^{-1} at the upper level; Figs. 4b and 5b). The asymmetric flow gives a rather complex structure of the inertio-gravity waves. The flow variation downstream is dominated by these waves and their constraint to surface conditions (see cross sections, Figs. 4c, d and 5c, d). Horizontally, an area of weak winds is found downstream the highest mountains (the wind shadow; Figs. 4a, b and 5a, b). In addition, there is an area of relatively strong winds to the right of the wind shadow (the right-side jet). Without friction, minimum wind speed in the shadow is found at the surface (0.8 ms^{-1}; Fig. 4a), while with friction, the minimum value is found close to the upper level (5.0 ms^{-1}; Fig. 5b).

The left-side jet and the upstream minimum are found at the same positions in the two experiments, positions that vary little with height. The positions of the downstream structures, on the other hand, are generally significantly different in the two experiments. The structures tilt with height, but in a different
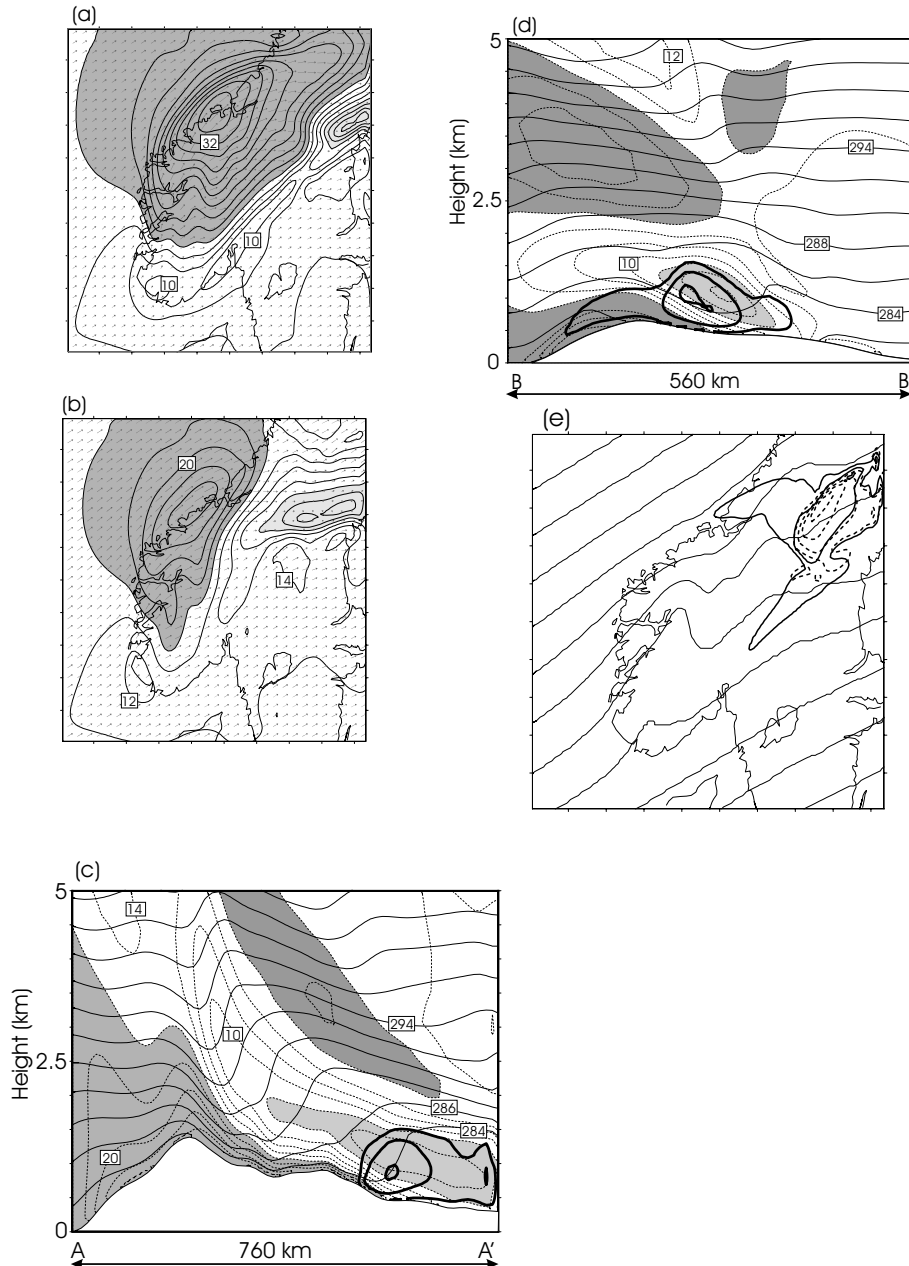
Fig 4. Results from simulations with $U = 15$ ms^{-1} without surface friction, but with rotation (U15S). The terrain is smoothed (see Fig. 1 and text for further details). (a) Wind vectors and isotachs every 2 ms^{-1} at the lowest model level. (b) As (a) but for a model level at about 630 m above ground level. (c) Vertical cross section along the flow showing isentropes (solid line; every 2 K), isotachs (broken line; every 2 ms^{-1}) and TKE (heavy line; every 1 m^2 s^{-2} starting on 0.5 m^2 s^{-2}). (d) As (c), but the cross section is taken across the flow. Positions of the cross sections are shown in Fig. 2a. (e) Isobars (slp) every 2.5 hPa and TKE at about 630 m above ground (broken lines; starting at 0.5 with contours 1.0 m^2 s^{-2}) and at about 280 m (solid lines) above ground.

way. The difference in the positions is smallest aloft (Figs. 4b and 5b). In both the experiments, a band with well-defined weak winds here connects the wind shadow and the upstream minimum. The right-side jet's position is slightly different. Another difference at the upper level is that the gradient in the wind speed between the left-side jet and the wind shadow is more gradual

without friction. With friction, this results in a secondary minimum over inner Trøndelag.

Without friction, the tilting inertio-gravity waves extend down to the surface. The cross sections (Figs. 4c, d) show that the waves tilt in the same direction as the lee-side mountain slopes, both along and across the main flow direction. Thus, the wave activity
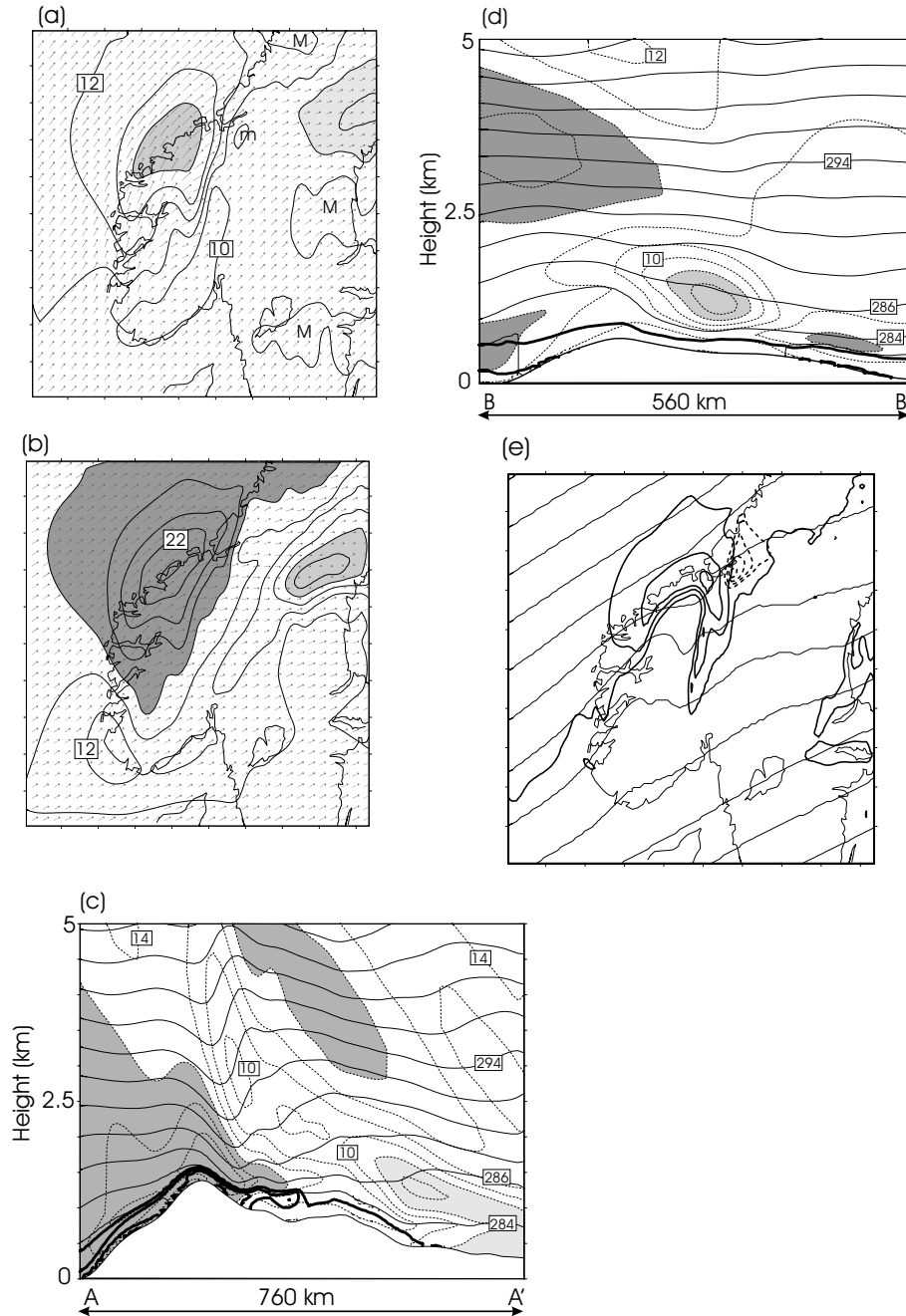
Fig 5. As Fig. 4, but results from an experiment having homogeneous surface friction (U15fS; $z_0 = 0.001$ m). TKE is contoured with an interval of 0.5 m² s⁻².

and the energy propagation have a component to the left across the flow. The cross-section across the flow shows a layer of weak winds tilting down to the surface (light shaded in Fig. 4d). Here, it forms the band of weak winds shown in Fig. 4a. An area of minimum wind speed is found above the ground downstream the highest mountains, north of the band with minimum wind speed at the surface. This minimum forms the wind shadow aloft. In the section along the flow (Fig. 4c), the shadow is seen as an area of weak wind tilting down to the surface at the right end of the section. The wind minimum is characterized by near vertical isentropes as a sign of breaking waves. TKE is here produced (see Figs. 4c–e).

Above the layer of weak winds, a layer with stronger winds is found. Also, this layer tilts down to the surface south of the wind shadow. Without friction, the band of strong winds extends to the surface (Fig. 4d), and the right-side jet might be interpreted

as winds belonging to this layer. With friction, such an extension is hardly present (Fig. 5d).

Comparing the cross-sections through the waves in the two runs (Figs. 4c, d and 5c, d), we see that friction not only forms a BL, but also damps the amplitude of the inertio-gravity waves. Consequently, friction reduces the upwards vertical flux of energy in the waves. In particular, with friction there is no longer any sign of wave breaking aloft. In this way, high values of TKE is only found in the BL.

With friction, the right-side jet appears as an area of maximum winds at the top of the BL (Fig. 5d). The minimum wind speed in the wind shadow at the surface is increased from 0.8 ms^{-1} without friction to 5.7 ms^{-1} when friction is included. This is most likely a result of mixing of momentum.

4.3. Results from linear flow at $U = 15$ ms^{-1}

Results from the linear model having no friction for $U = 15$ ms^{-1} are shown in Fig. 6 for smoothed terrain. Note that the geographical area is extended towards east and north. The linearized wind speed (linear terms of $(U + u)^2$, see Appendix) at the surface (Fig. 6a) shows a distribution much in agreement with the nonlinear run without surface friction (U15S). The core of the left-side jet and the upstream minimum are approximately at the same positions, but the amplitude of the wind maximum is less (25.8 ms^{-1}, compared to 36.2 ms^{-1} in U15S).

Also downstream the mountain crest, the structure of the linear wind speed is similar to the nonlinear case. We find a wind shadow much as in U15S at the surface, and a band of weak winds between the wind shadow and the upstream minimum. However two significant discrepancies appear; (1) In the wind shadow, the linear model predicts a far shallower structure. The difference is associated with the breaking waves, a nonlinear behaviour. (2) The axis of the wind shadow at the ground (along several wind minimums downstream) is more towards north than in the similar nonlinear run (compare Fig. 6a to Fig. 4a). Minimum linear wind speed is 5 ms^{-1} in the wind shadow, compared to 2.2 ms^{-1} in the nonlinear case, both found at the ground level. A weak signal from the right-side jet is present in both models.

From the surface map (Fig. 6a), we clearly see wave signals propagating northeastwards. Vertical cross sections, across and along the flow (Figs. 6b and c), show similar inertio-gravity waves as in the nonlinear case (U15S).

The results from the linear model might be summed up from Fig. 7, which shows the wind variation with height for wind extremes connected to the mesoscale structures for linear and nonlinear flows ($U = 15$ ms^{-1}). While the structures upstream the crest behave linearly, the downwind wind shadow behind is considerably affected by nonlinear processes. Accordingly, the left-side jet and the upstream minimum show a better fit than the wind shadow. Only a small discrepancy is found here close to the ground. Worth noting is that the position of the
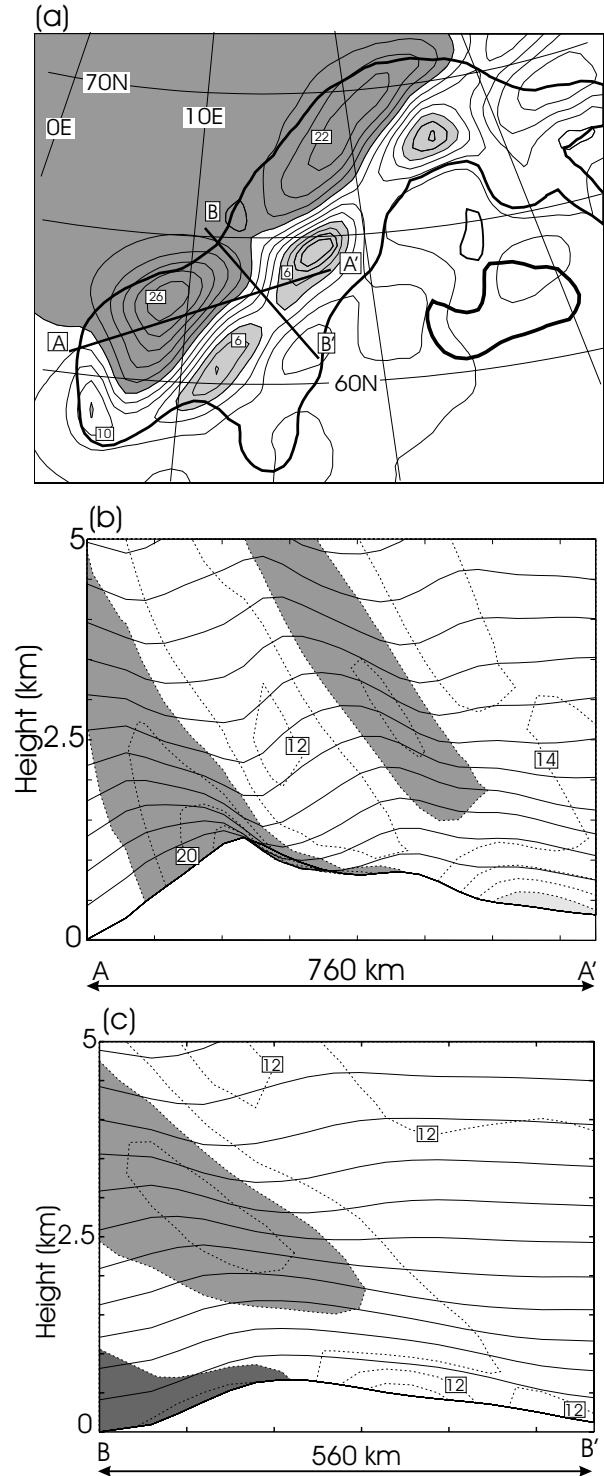

Fig 6. Results from the linear model for $U = 15$ ms^{-1}. (a) Linear isotachs (2 ms^{-1} interval) at ground level. (b) Linear isotachs and density contours (every 0.05 kgm^{-3}) for a vertical cross-section along the flow showing the wind shadow. (c) As (b) but across the flow. The positions of the cross-sections are as indicated in Figs. 6a or 2a.
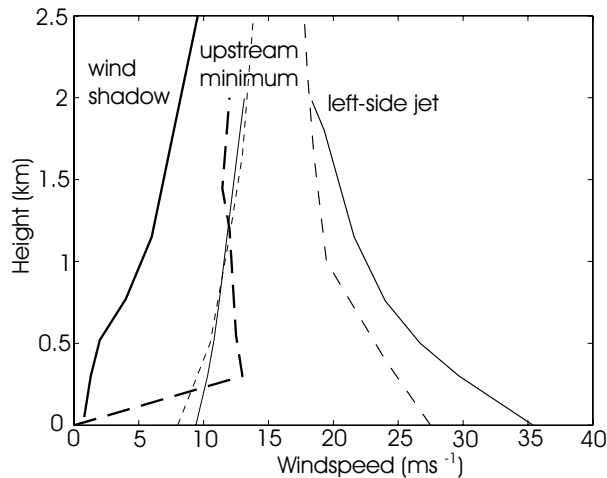
Fig 7. Variation of wind speed with height for three mesoscale structures for a background wind speed of 15 ms^{-1}. Broken lines give results from a linear model (linear wind speed) and solid lines from a nonlinear experiment without surface friction. Thick lines represent the downstream wind shadow, thin lines the upstream minimum and normal lines the left-side jet.

structures may differ a little, and consequently the height above ground.

4.4. Dependence of downstream structures on wind speed

We will briefly describe how the downstream features vary with wind speed. As discussed in BG05, ray-tracing techniques may be used to estimate the linear wave length of the inertio-gravity waves (their eq. 1). It typically varies with Ro, which means U in our case since f and L are regarded as constants. Accordingly, the downstream wind shadow is found further downstream as the large-scale wind speed increases. In the nonlinear case of $U = 22.5$ ms^{-1}, it starts at the boundary of the inner integration area and extends into the outer area. We therefore present results from the outer integration area.

Figure 8a shows the position of the shadow at the surface—indicated with selected isotachs (speed-up)—for experiments U10S, U15S and U225S, all without surface friction. Figure 8b shows a cross-section along the shadow with TKE and two phase lines of the inertio-gravity waves for the same experiments. The first phase line is for minimum wind speed associated with the shadow and the second for maximum wind speed in the layer above. Horizontal and vertical distances between the two phase-lines give half the wavelengths.

The wavelengths increase with background wind speed. Consequently, the position of the shadow moves downstream with stronger wind speeds. For all wind speeds, large values of TKE are found in the interior of the flow as a sign of breaking waves. Maximum TKE is found along the phase for minimum wind, a
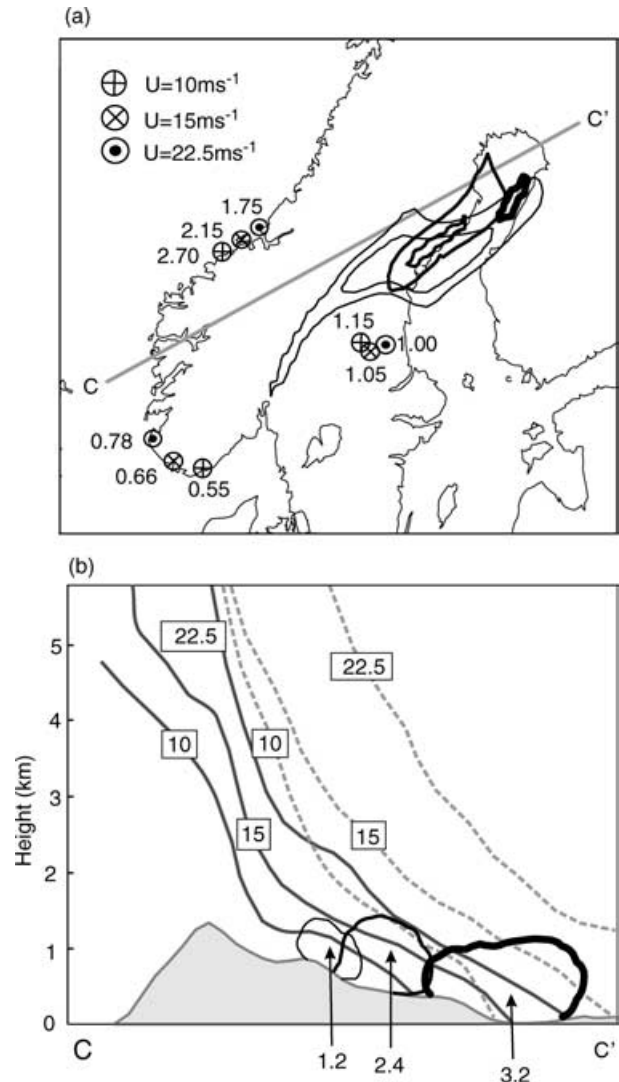

Fig 8. (a) Contours of speed-up at the surface level in an experiment without surface friction (*UXX*S). Speed-up contours are 0.3 and 0.5 for $U = 10$ (thin line), $U = 15$ ms^{-1} (medium line). For $U = 22.5$ ms^{-1} (heavy line), only 0.5 speed-up is depicted. The positions and the speed-ups of the other mesoscale structures are indicated. (b) Cross section (for position see a) along the wind shadow showing phase lines of inertio-gravity waves. Solid lines are phase lines of minimum wind speed towards the wind shadow. Stippled lines are phase lines for maximum wind speed above the layer of weak winds. The 0.5 m^2 s^{-2} contours of TKE with the numeric value of maximum TKE are shown.

little above the surface and just upstream of the position of minimum wind speed in the shadow (Fig. 8b). TKE increases with wind speed.

The positions of maximum wind speed (or speed-up) in the right-side jet do not vary much with large-scale wind speed. In other words, while the wind shadow is displaced in the rear as wind speed increases, the right-side jet stays nearly fixed. This means that the right-side jet is not directly linked to the
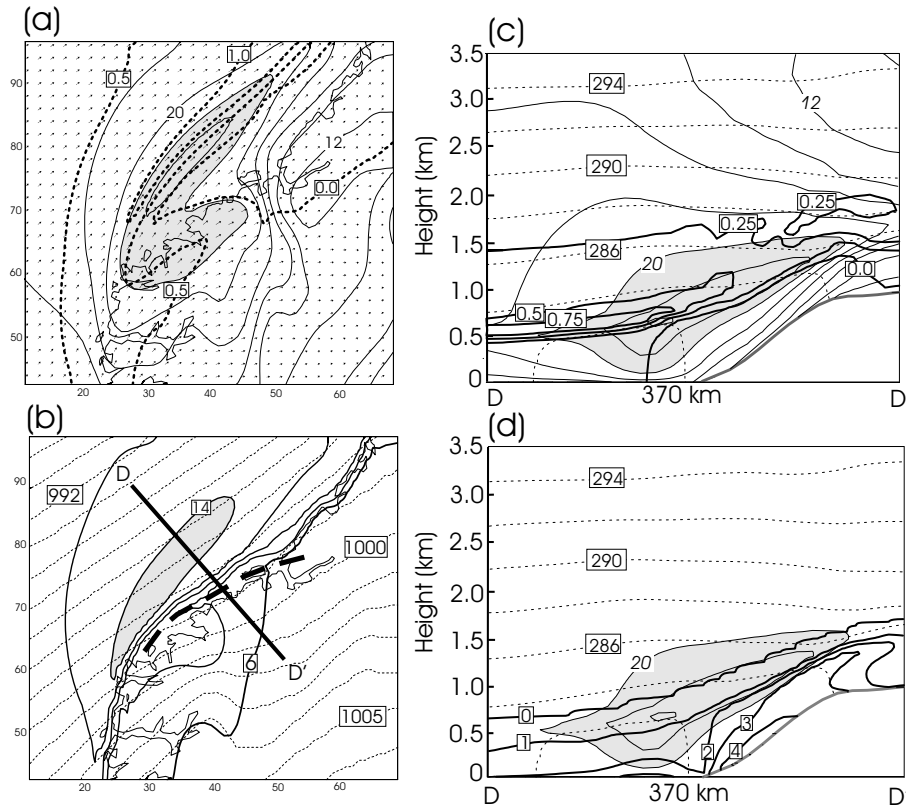
Fig 9. Flow in the area Stadt-Trondheimsfjord in an experiment with differential surface friction and background wind speed 15 ms^{-1}. (a) Wind vectors and wind speed (isotachs every 2 ms^{-1}) and PV (heavy contours every 0.5 PVU) at 640 m above ground. Areas with wind speed stronger than 22 ms^{-1} are grey-shaded. (b) Sea level pressure (stippled isobars every 1 hPa) and wind speed at lowest model level (isotachs every 2 ms^{-1}). An area with wind speed stronger than 14 ms^{-1} is shaded. A heavy, stippled line indicates a trough in wind speed at the coast. (c) Cross section D–D′ (for position see b); isentropes every 2 K, wind speed (stippled isotachs every 2 ms^{-1}), an area with wind speed stronger than 20 ms^{-1} is shaded; PV (heavy contours every 0.25 PVU). (d) Same as (c), but TKE (every 1 m^2 s^{-2}) instead of PV. Isotachs less than 20 ms^{-1} are omitted.

wind shadow. In accordance with the results in the linear model (Fig. 6), we find a second area of increased wind speed further downstream to the right of the shadow (not shown). The positions of maximum wind speed in the left-side jet move downstream as the background wind speed is increased (Fig. 8a). Likewise, the minimum wind speed of the upstream minimum moves to the left due to lesser influence of rotation. This is in accordance with results in BG05.

The nonlinear behaviour of the wind shadow is evident from low-level breaking resulting in dissipation (TKE; Figs 4c, e). Surprisingly enough, the wave breaking does not cease when the background wind speed increases. It only results in moving the breaking area downstream (Fig. 8). Scaled with the background wind speed, the turbulent intensity remains fairly constant. We have not generally addressed how such wave breaking depends on other flow parameters and mountain shapes. Nor have we identified the true dynamical reason why the breaking takes place. Our wake, heavily influenced by breaking inertio-gravity

waves, must be classified differently than classical wakes. Similar wind shadows should be frequent at several places around the world. Elaboration on these matters is left for future work.

4.5. The influence of differential friction

In order to study the origin of the coastal wind shadow north of Stadt identified in BG05, we have made simulations with differential surface friction. The flow in the area north of Stadt is shown in Fig. 9 for U15dfS. The figure shows the flow at the upper level (a: wind vectors, wind speed, PV) and at the surface (b: slp, wind speed), and in a cross-section across the left-side jet and the coast (c: θ, wind speed and PV; d: θ, wind speed and TKE). Figs. 9a, b should be compared with Figs. 5a, b for homogeneous friction.

Compared with experiments with homogenous friction, differential friction between land and ocean naturally has a large effect on the flow. As expected, the effect is first of all large in the

BL, and particularly in coastal areas. Stronger friction over land gives stronger damping of the inertio-gravity waves than with homogeneous weaker friction. However, the structure of waves, positions and amplitudes of the downstream extremes does not change very much (see Table 2).

The left-side jet is very much affected. At surface, the position of the left-side jet is now found over sea—where friction is low—outside the coast north of Stadt. Differential friction also results in a more elongated structure of the jet (Figs. 9a, b). A trough with minimum wind speed is found at the coast from Trondheimsfjord towards Stadt (Fig. 9a). The wind direction is here along the trough. In BG05, we found a similar wind structure that we called the coastal wind shadow. The wind shear in the jet is very strong towards the coast, in particular towards the coastal wind shadow just north of Stadt.

As discussed in BG05, differential friction causes significant coastal convergence at the coast south of Stadt. However, north of the Stadt the convergence disappears or changes sign to divergence (not shown). The strong shear towards the coast gives negative absolute vorticity in the BL around the corner Stadt and further northeastwards along the coast north of Stadt (not shown). Associated with this, weak negative PV is found in the BL from the core of the jet to the coast and further over the mountain slopes (Fig. 9c). The negative PV, not seen in the experiments with homogeneous friction or without friction, might be a sign of symmetric instability. However, negative PV is only found in the BL, where friction is high (visualized with high TKE in Fig. 9d). Using TKE as a possible measure of instability, we only find instabilities (large values of TKE) over the steepest mountains.

The upper level is still influenced by the differential friction since we find two maxima in the wind speed; one over land and one over sea (Fig. 9a). Also, at this level slightly negative PV is found. Above this level, the maximum over the sea disappears, and the jet is found above the coast, much as in the experiment with homogeneous friction (Figs. 5a, b).

We have shown that the coastal wind shadow first of all is an effect of differential friction. In BG05, the shadow was also thought to be connected with increased upstream dissipation connected to the steep lee side of the mountains. With the less steep mountains in experiments *UXX*dfS, however, the wave activity, in combination with upstream TKE, seems to deepen the BL, giving slower winds at low levels (Fig. 9d). The increased TKE is probably due to large vertical shear at the lee slopes below the jet aloft (Fig. 9d). Negative PV is found in the same area (Figs. 9b, c). However, in the presence of surface friction no symmetric instability takes place.

5. Further discussions using linear theory

In many respects the linear model gave realistic results. Further discussion using linear theory is now given for vertical energy fluxes (5.1), the right-side jet (5.2) and for the impact of surface friction (5.3).

5.1. Vertical energy fluxes

In the literature as well as in weather forecasting models, the hydrostatic wave drag excited on the atmosphere by the mountain—discussed in terms of linear wave drag—has been thoroughly studied (e.g. Lott and Miller, 1997). Using the linear model, we have integrated the wave energy $\langle \rho_0 pw \rangle$ (p and w are perturbations in the linear model) over an area enclosed by the outer domain (Section 3) of the nonlinear model simulations. Fig. 10 shows how the wave energy transport decreases with height in the linear results for $U = 15$. In the case without rotation (solid line), the 3-D dispersive effect steadily decreases the integrated wave energy with height. Ideally, the wave energy should be constant with height (Eliassen and Palm, 1960), but our integration takes place in a limited area. Aloft some wave energy escapes the integration area. The broken line shows the similar case with rotation included in the linear model. The energy is then reduced at the surface, and above 2 km the wave energy drops quickly. This is in accordance with Smith (1979).

Above 2 km, there is only a slight decline in energy transport with height. The sharp drop near the ground is due to the limited vertical propagation depth (D) of inertio-gravity waves. While flow components heavily influenced by the Coriolis effect (evanescent solutions) are limited to D, the shorter wave components (propagating waves) continue upwards. D may be estimated according to Pierrehumbert (1986) and Gill (1982) as

$$D = Ro/m_{ks} \tag{2}$$

where m_{ks} is the hydrostatic vertical wave number, which in 2-D flow is of order of N/U. Using $Ro \sim 1$, $U = 15 \, \text{ms}^{-1}$ and $N = 0.012 \, \text{s}^{-1}$, the D is about 1–2 km, a result that agrees well with Fig. 10.

5.2. The right-side jet

In our nonlinear experiments with smoothed topography, the right-side jet appeared well downstream of the main massif to the right of the wind shadow (see Table 2; Figs. 3 and 4). Generally, the signal is not particularly strong, but represents a pronounced contrast to the wind deficit in the shadow.

We have looked more carefully into the feature by letting our standard flow with $U = 15 \, \text{ms}^{-1}$ pass a circular cosine shaped mountain with 150-km total length, both in the nonlinear and in the linear model. The nonlinear model indicates a speed-up of about 1.3 for the right-side jet, a little more than over real mountains (Table 2). The linear model shows a similar feature with a weaker signal (speed-up 1.1).

The nature of the jet might be explained in the framework of the linear model. In Fig. 11a, the linear flow—without
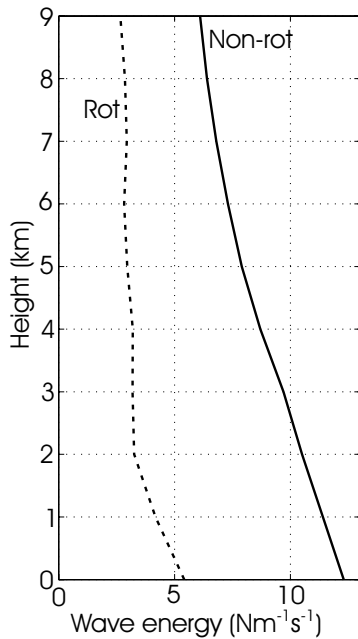
Fig 10. Mean vertically propagating wave energy in the linear model for an area equal to the outer domain in the nonlinear model. The broken line shows the case with rotation included and the solid line the case having no rotation.

friction—generates pressure perturbations indicated as solid lines over the mountain (the 50-m contour of the mountain height is indicated with a broken line). The upstream wind minimum, and the left-side wind maximum are indicated together with the positions of the downstream wind extremes. One trajectory at the surface level is shown, ending in the right-side jet maximum. The cross-flow wind component (v) is indicated as vectors along the trajectory. Following the trajectory upstream the mountain, the deceleration is associated with deflection to the right caused by the high pressure. Behind the mountain, the lee-side low-pressure area attracts the air parcel towards the centre line. This positive cross-flow component is acted upon by a Coriolis force to increase the along-flow wind component.

In nonlinear flows, the acceleration along a trajectory (Du_s/Dt) is due to cross-flow ageostrophic flow, $Du_s/Dt = fv_{an}$. Here u_s is the wind speed in the direction along the trajectory and v_{an} is the ageostrophic wind component across. In linear, steady-state flow, however, we write the relation as a three-way balance between normalized perturbed pressure ($\nabla_H p$), Coriolis force on perturbation ($f\vec{k} \times \vec{u}$) and advection of inertia ($\vec{U} \cdot \nabla_H \vec{u}$) (see Appendix). Aligning the coordinate system with the background flow ($\vec{U}$) and integrating over a characteristic length of the disturbance (L), we find the accumulated Coriolis contribution (ACC) to be
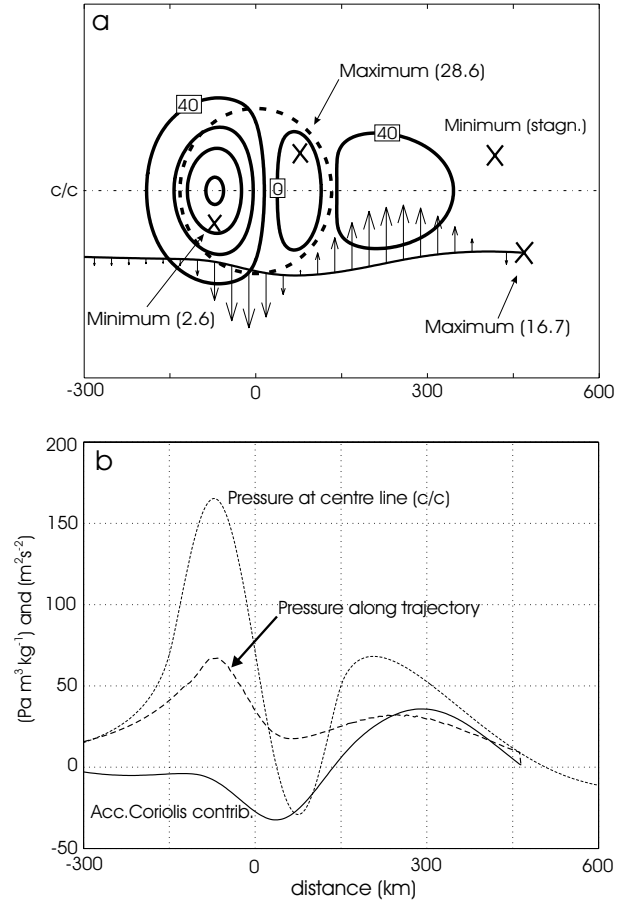
$$ACC = \int_{-L}^{0} fv \; dL, \tag{3}$$

Fig 11. (a) Surface pressure perturbations (isobars, 40 Pa interval) generated by a flow with $U = 15 \text{ ms}^{-1}$ passing a cosine-shaped mountain ($a_x/a_y = 150 \text{ km}/150 \text{ km}$, $H_m = 1500 \text{ m}$). The dotted line shows the 50 m terrain contour. Maximum and minimum wind speeds are labelled with respective numeric values (ms^{-1}). The trajectory at the surface of a parcel ending in the right-side jet core is shown. Arrows indicate cross-flow winds (v). Axes indicate horizontal distances. (b) Pressure perturbations and accumulated contribution of the Coriolis force (ACC).

where L is the length scale associated with the disturbance. We depict ACC along the trajectory in Fig. 11a as seen in Fig. 11b (solid line). From Fig. 11b, we see that around the mountain-top, the Coriolis force slows down the along-flow component, while a bit further downstream there is a positive contribution. Still further down the trajectory, at the point where ACC again changes sign, the parcel reaches its maximum wind speed. Worth mentioning is that the wind maximum is well downstream of the minimum pressure at the centre line (see broken line in Fig. 11b). From this, we see that the right-side jet is tied to the low-pressure anomaly, and not directly to the wind minimum. The contribution of ACC to the along-flow component may be estimated by normalizing the value in Fig. 11b by U. The lifting is relatively weak this far away of the mountains, so we expect ACC to mainly balance the inertia. Thus, we find that the Coriolis force

contributes at most to about $30\,\mathrm{m^2\,s^{-2}}/15\,\mathrm{ms^{-1}} = 2\,\mathrm{ms^{-1}}$ in the along-flow direction.

Doyle and Shapiro (1999) identified a jet at the tip of Greenland that they called a 'tip jet'. Their jet is a direct result of a low pressure generated behind the mountain, pulling air around the tip. This can be seen arguing from a Bernoulli principle: A parcel next to the lower boundary passes the tip of Greenland and encounters a sudden drop in pressure, which allows the wind speed to raise immediately. The right-side jet identified in this paper is also generated by the low pressure behind the mountain, but arises secondarily through the Coriolis effect on the cross-flow wind component. The different scales involved separate the nature of these two jets.

We have shown that the right-side jet arises in inviscid flows, and therefore can be explained in absence of dissipation. However, we have found that nonlinear results give a little larger speed-up. Thus we expect nonlinear effects to contribute to the feature.

When the background wind speed increases beyond $U = 15\,\mathrm{ms^{-1}}$, the right-side jet becomes less pronounced (see Table 2). This means that the signal decreases with increasing Ro. There is, however, increased wind speed to the right of the downwind low-pressure area in all the simulations.

5.3. The impact of surface friction

Even with a short roughness length, surface friction in nonlinear simulations had a considerable impact on the flow. The vertical displacements of the isentropes were reduced and consequently the surface pressure perturbations. Clearly, inclusion of surface friction suppresses wave breaking in the inertio-gravity waves. The turbulence was confined to the BL. Accordingly, no associated turbulence was present aloft in the wind shadow (Figs. 5c–e). Downstream the highest mountains the BL was, however, rather deep and increased TKE was detected in the BL (Fig. 5e).

Naturally, friction damped the amplitudes of the left-side jet considerably (compare Figs. 4 and 5, see also experiments UXXS and UXXfS for the three speeds XX in Table 2). Also, the amplitude of the downstream wind shadow was reduced, i.e. the wind speeds became stronger. The amplitudes of the upstream minimum and the right-side jet were, however, only slightly affected. The positions of the structures did not change much with friction, except for the downstream wind shadow. Here, the tilting of the structure across the flow disappeared, i.e. the structure got approximately the same position at the surface and at the top of the BL. Clearly, the damping of the wave amplitudes and the mixing of momentum in the tilting structures increased the wind speed of the shadow considerably.

The damped amplitudes of the inertio-gravity waves and the reduced pressure perturbations indicate that friction reduces the effective height of the mountains. This means that friction prevents upstream stagnation when the large-scale wind speed is decreased. When friction is included, it seems appropriate to evaluate the presence of stagnation at the top of the BL. For cases with friction in Table 2, speed-ups of the upstream minimum are given for a fixed layer a little into the BL (640 m above ground). For cases without friction, the numbers are given for the ground. Therefore, comparison of the numbers with and without friction in Table 2 should be done with caution.

In order to identify linear and nonlinear effects of surface friction, we will do an attempt to introduce friction in the linear theory. Recently, Smith et al. (2005) derived a new linear theory on wave absorption in BLs and applied the theory for downstream propagating lee waves. In a coming paper by Smith (R.B. Smith personal communication), he discusses how the theory applies for vertically propagating mountain waves. According to him, the 1-D, non-rotating, linear Boussinesq flow might be represented by the formulas below, where $(U_b + u_b)$ is the wind speed in the BL and $(U + u)$ the wind speed in the free atmosphere above:

$$U_b\, du_b/dx = -dp/dx - C_b u_b + C_t(u - u_b) \qquad (4)$$

$$U\, du/dx = -dp/dx. \qquad (5)$$

p is the normalized pressure perturbation generated in the free atmosphere penetrating through the BL, (see Appendix). C_b is a friction coefficient for linear friction in the BL. C_t is the coefficient controlling the exchange of momentum with the free atmosphere. The vertical velocity at the top of the BL (w_T) is a sum of lifting near the lower boundary (w_G) and modification by BL effects:

$$w_T = w_G + w_B = \vec{U}_B \cdot \nabla h(x, y) - H\nabla \cdot \vec{u}_B(x, y), \qquad (6)$$

where the flow is extended to three dimensions and the continuity equation is vertically integrated in the BL. H is the height of the BL. Transformed into the Fourier space, the displacement at the top of the BL is

$$\hat{\eta} = \hat{h} - \frac{H}{\sigma_B}(k\hat{u}_B + l\hat{v}_B), \qquad (7)$$

where $\sigma = Uk + Vl$ is the intrinsic frequency and $\hat{h}(k, l)$ the Fourier transformed terrain. (u_B, v_B) are found from manipulating 2-D versions of (4) and (5) and an equation for pressure in the free atmosphere (see Appendix). We write the effective displacement above the BL as

$$\hat{\eta} = \frac{\hat{h}}{1 - \frac{iN^2H(i\sigma + C_T)}{\sigma\sigma_B m(i\sigma + C_B + C_T)}(k^2 + l^2)}. \qquad (8)$$

From (7), we see that divergence in the BL contribute to a damping of wave amplitudes above the BL. In addition, estimation of (8) shows that surface friction tends to shift the disturbance upstream. This is in agreement with Smith et al. (2005) and with a coming paper by R. B. with Smith, (personal communication).

In order to demonstrate the effect of surface friction included in the linear model, we show a cross-section (A–A′)
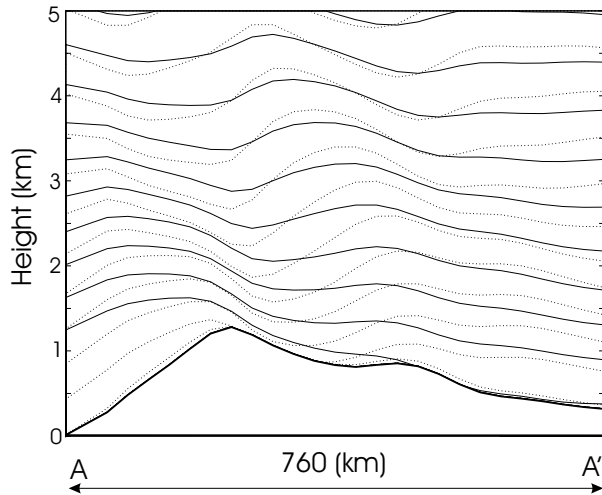
Fig 12. Cross section showing density contours (every 0.05 kg m^{-3}) along the flow (A–A′ in Fig. 2a) for the same conditions as in Fig. 6, but including BL effects ($H = 729$ m, $C_t = 0.005$ s^{-1}, $C_b = 0.0028$ s^{-1} $(U_b, V_b) = (8.36, 4.82$ ms^{-1})). Solid line indicates solution with BL effects, dotted line solution as in Fig. 6b.

comparing density anomalies with (solid) and without (dotted) friction (Fig. 12). We see that the density anomalies are considerably dampened when friction is included. In case the Coriolis force is included in the linear BL theory, we expect further divergence in the BL, and subsequently more damping.

6. Conclusions

In this paper, we have broadened the understanding of mesoscale structures as identified and described by BG05. First of all, the effects of surface friction and wave breaking have been considered. The study has been based on simulations with a numerical model from idealized atmospheric states with a constant background wind direction from southwest and a constant stable stratification in the troposphere. The results were compared with computations from a linear 3-D model with rotation included.

A few experiments without rotation and surface friction showed a regime change to a flow characterized by upstream stagnation and a downstream classical wake for effective mountain heights (h) higher than the order of one. In accordance with earlier work (BG05), all experiments with rotation included showed an asymmetric flow with a left-side jet and an upstream wind minimum on the right side. For all wind speeds, the flow belonged to the same flow regime characterized with a flow over the mountains and inertio-gravity waves propagating downstream. Also in this regard, the results agreed with BG05.

All experiments with rotation included showed a downstream wind shadow with minimum speed-up increasing with increasing background wind speed. From the experiments on the largest integration area, we clearly saw that the wind shadow is the first minimum at the surface in downstream inertio-gravity waves. As the wavelengths increased with increased background wind

speed, the wind shadow was displaced downstream. The experiments without surface friction showed clear signs of breaking waves—high levels of TKE connected to the shadow. The wave breaking contributed to the formation of the wind shadow. The level of TKE increased with background wind speed. The downstream wind shadow, caused by rotational effects, might be considered as a new kind of a wake that should be frequent at other places in the world.

Comparison of results from experiments without surface friction with results from linear theory showed that the flow is rather linear upstream the main crest (upstream minimum and left-side jet) and aloft. The character of the downstream wind shadow was, however, found to be highly nonlinear. We assign this to dissipation through extensive wave breaking and associated turbulence. The nonlinear effects were necessary to get the right position, depth and strength of the shadow.

Even friction with the short roughness length of the ocean caused considerable effects on the flow and the mesoscale structures. The left-side jet became considerably weaker and the downstream wind shadow less pronounced. The wind speed of the upstream minimum was less affected. Friction damped the amplitudes of the inertio-gravity waves. Wave breaking ceased and turbulence was confined to the BL only. As the large-scale wind speed was increased, naturally, the damping of the waves was reduced. The experiments and an attempt to add friction in the linear computations showed that friction resulted in a lower effective mountain height. In this way, a regime change with upstream stagnation and flow around the mountains is prevented as the background wind speed is reduced (lower $\hat{h}$).

In accordance with BG05, increased wind speeds were found on the right side of the wind shadow (right-side jet). The position did not change much as the wind speed increased and the wind shadow was displaced downstream. The origin of the jet could be explained from linear theory. Cross-flow winds towards the low-pressure perturbation in the lee of the mountains, assisted by the Coriolis force, generated increased wind speed along the flow a little further downstream.

The coastal wind shadow mentioned in BG05 was simulated with smoothed topography and differential friction between land and sea. Without differential friction, no coastal wind shadow was found. Downstream the steep mountain slopes of Møre, PV became negative in the BL due to the large shear between the left-side jet and the coastal minimum. However, no sign of any instability was seen.

In this paper, we have studied idealized flows with no heat effects. A more complex picture is expected in realistic atmospheric conditions. Inclusion of humidity, condensation and release of latent heat might, for instance, complicate the mountain flow considerably. The simplicity, however, allowed us to draw more rigorous conclusions.

While the upstream structures were verified by observations in BG05, no strong observational evidence has been documented for the downstream features. This important task is left for

future investigations. Observed evidence for the downstream wind shadows is particularly needed from both southern Norway and similar mountains elsewhere. Observational studies should be combined with theoretical studies to understand the dynamical nature of such structures.

7. Acknowledgments

8. Appendix A

A1 Linear model

The horizontal component of the linearized Boussinesq approximated momentum equation may be written as

$$\frac{\partial \vec{u}}{\partial t} + \vec{U} \cdot \nabla_H \vec{u} - f\vec{k} \times \vec{u} = -\frac{1}{\rho_0}\nabla_H p \qquad (A1)$$

and the vertical as

$$\frac{\partial w}{\partial t} + \vec{U} \cdot \nabla_H w = -\frac{1}{\rho_0}\frac{\partial p}{\partial z} - b, \qquad (A2)$$

where the upper case denotes the constant background part of the variable. The lower case denotes the perturbed part. The variable b is the buoyancy $b(x, y, z, t) = g\rho'(x, y, z, t)/\rho_0$. The rest follows standard notation. In order to get a closed system, we add the continuity and buoyancy equation,

$$\nabla \cdot \vec{u} = 0 \qquad (A3)$$

$$\frac{\partial b}{\partial t} + \vec{U} \cdot \nabla_H b + N^2 w = 0 \qquad (A4)$$

and applying the linearized boundary condition, connecting the vertical velocity (w) and the fluid displacement (η),

$$\frac{\partial \eta}{\partial t} + \vec{U} \cdot \nabla_H \eta = w. \qquad (A5)$$

We transfer the equations into Fourier space ($\vec{U} \cdot \nabla \rightarrow i\sigma$) assuming steady state. By using simple algebra, and solving an ordinary differential equation, the fluid displacement becomes

$$\hat{\eta}(k, l) = \hat{h}e^{imz}, \qquad (A6)$$

where $\hat{h}$ is the Fourier transformed terrain (see Smith, 2001).

The rest of the variables in the Fourier space turn out to be

$$\hat{w}(k, l) = i\sigma \hat{\eta} \qquad (A7)$$

$$\hat{b}(k, l) = N^2 \hat{\eta} \qquad (A8)$$

$$\hat{p}(k, l) = \left(\frac{i\hat{\eta}}{m}\right)(N^2 - \sigma^2) \qquad (A9)$$

$$\hat{u}(k, l) = \frac{-m(\sigma k - ilf)i\hat{\eta}}{k^2 + l^2} \qquad (A10)$$

$$\hat{v}(k, l) = \frac{-m(\sigma l + ikf)i\hat{\eta}}{k^2 + l^2}, \qquad (A11)$$

where the non-hydrostatic vertical wave number including rotation is

$$m^2 = \frac{N^2 - \sigma^2}{\sigma^2 - f^2}(k^2 + l^2), \qquad (A12)$$

$\sigma = Uk + Vl$ is the intrinsic frequency, (k, l) is the horizontal wave numbers.

A2 Linearized wind speed

Dividing wind into background and perturbed parts allows us to write the wind speed as

$$[(U + u)^2 + (V + v)^2]^{1/2}. \qquad (A13)$$

Aligning the coordinate system with the background flow, V vanishes,

$$[(U + u)^2 + v^2]^{1/2}. \qquad (A14)$$

According to basic assumptions in linear theory, products of the perturbations are neglected, so that (A14) is

$$\text{linearized windspeed} = (U^2 + 2U \cdot u)^{1/2} \approx |\vec{U} + \vec{u}|. \qquad (A15)$$

Thus, the linearized wind speed is the perturbation aligned with the background flow, added to the background flow. The linearized wind speed is always less or equal to the full nonlinear wind speed. As the nonlinearity increases, the approximation error in (A15) increases accordingly. For the same reason, the linear theory becomes less accurate.

References

Barstad, I. and Grønås, S. 2005. Southwesterly flows over southern Norway-mesoscale sensitivity to large-scale wind direction and speed. *Tellus* **57A**, 136–152.

Burk, S. and Thompson, H. 1989. A vertically nested regional numerical prediction model with second-order closure physics. *Mon. Wea. Rev.* **117**, 2305–2324.

Doyle, J. D. and Shapiro, M. A. 1999. Flow response to large-scale topography: the Greeland tip jet. *Tellus* **51A**, 728–748.

Eliassen, A. and Palm, E. 1960. On the transfer of energy in the stationary mountain waves. *Geofys. Publ.* **22**, 1–23.

Gill, A. E. 1982. *Atmosphere-Ocean Dynamics*. International Geophysics series, Academic Press, NY, 662.

Grell, G., Dudhia, J. and Stauffer, D. 1994. *A Description of the Fifth-Generation Penn State/NCAR Mesoscale Model (MM5)*. NCAR technical note NCAR/TNN-398+STR, Boulder, CO, U.S.A.

Grubišić, V., Smith, R. B. and Schär, C. 1995. The effect of bottom friction on shallow-water flow past an isolated obstacle. *J. Atmos. Sci.* **50**, 1985–2005.

Klemp, J. B. and Lilly, D. K. 1978. Numerical Simulation of Hydrostatic Mountain Waves. *J. Atmos. Sci.* **35**, 78–107.

Lott, F. and Miller, M. J. 1997. A new subgrid-scale orographic drag parameterization: Its formulation and testing. *Quart. J. R. Met. Soc.* **123**, 101–127.

Ólafsson, H. 2000. The impact of flow regimes on asymmetry of orographic drag at moderate and low Rossby numbers. *Tellus* **52A**, 365–379.

Ólafsson, H. and Bougeault, P. 1997. The effect of rotation and surface friction on orographic drag. *J. Atmos. Sci.* **54**, 193–210.

Peng, M. S., Li, S.-W., Chang, S. W. and Williams, R. T. 1995. Flow over mountains: coriolis force, transient troughs and three dimensionality. *Q.J.R. Meteorol. Soc.* **121**, 593–613.

Pierrehumbert, R. T. 1986. Chapter 21 in Mesoscale meteorology and forecasting (ed. P. S. Ray), Publ. American Meteorological Society, Boston.

Pierrehumbert, R. and Wyman, B. 1985. Upstream effects of Mesoscale Mountains. *J. Atmos. Sci.* **42**, 977–1003.

Schneider, T., Held, I. M. and Garner, S. T. 2003. Boundary Effects in Potential Vorticity Dynamics. *J. Atmos. Sci.* **60**, 1024–1040.

Schär, C., 1993. A generalization of Bernoulli Theorem, *J. Atmos. Sci.* **50**, 1437–1443.

Schär, C. and Smith, R. B. 1993. Shallow water flow past isolated topography. Part I: Vorticity production and wake formation. *J. Atmos. Sci.* **50**, 1373–1400.

Schär, C., Sprenger, M., Lüthi, D., Jiang, Q., Smith, R. B. and Benoit, R. 2003. Structure and dynamics of an Alpine potential-vorticity banner. *Q.J.R. Meteorol. Soc.* **129**(Part B), 825–855.

Smith, R. B. 1979. The influence of the Earth's rotation on mountain wave drag. *J. Atmos. Sci.* **36**, 177–180.

Smith, R. B. 1989a. Hydrostatic airflow over mountains. *Adv. Geophys.* **31**, 59–81.

Smith, R. B. 1989b. Comment on "Low Froude number flow past three dimensional obstacles. Part I: Baroclinically generated lee vorticies" byP. K. Smolarkiewicz and R. Rotunno. *J. Atmos. Sci.* **46**, 3611–3613.

Smith, R. B. 2001. Stratified airflow over Mountains, Ch.6 in *Environmental Stratified Flows*. Vol. 3. In: *Topics in Environmental Fluid Mechanics* (ed. R. Grimshaw), Kluwer Publishing, Boston.

Smith, R. B. and Grønås, S. 1993. Stagnation points and bifurcation in 3-D mountain flow. *Tellus* **45A**, 28–43.

Smith, R. B., Jiang, Q. and Doyle J. D. 2005. A theory of gravity wave absorption in boundary layer. *J. Atmos. Sci.*, in press.

Smolarkiewicz, P. K. and Rotunno, R. 1989. Low froude number past three-dimensional obstacles. Part I: Baroclinically generated lee vortices. *J. Atmos. Sci.* **46**, 1154–1164.

Thorsteinsson, S. and Sigurdsson, S. 1996. Orogenic blocking and deflection of stratified air flow over an f-plane. *Tellus* **48A**, 578–583.

Trüb, J. and Davies, H. 1995. Flow over mesoscale ridge: pathways to regime transition. *Tellus* **47A**, 502–524.